Journal Pre-proof

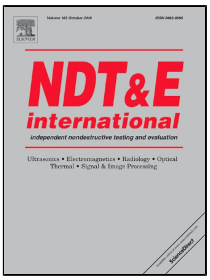

Vibrothermographic spectroscopy with thermal latency compensation for effective identification of local defect resonance frequencies of a CFRP with BVID

Saeid Hedayatrasa, Joost Segers, Gaétan Poelman, Erik Verboven, Wim Van Paepegem, Mathias Kersemans

PII:	S0963-8695(19)30306-8
DOI:	https://doi.org/10.1016/j.ndteint.2019.102179
Reference:	JNDT 102179
To appear in:	*NDT and E International*
Received Date:	27 May 2019
Accepted Date:	19 October 2019

Please cite this article as: Saeid Hedayatrasa, Joost Segers, Gaétan Poelman, Erik Verboven, Wim Van Paepegem, Mathias Kersemans, Vibrothermographic spectroscopy with thermal latency compensation for effective identification of local defect resonance frequencies of a CFRP with BVID, *NDT and E International* (2019), https://doi.org/10.1016/j.ndteint.2019.102179

Vibrothermographic spectroscopy with thermal latency compensation for effective identification of local defect resonance frequencies of a CFRP with BVID

Saeid Hedayatrasa [1,2*], Joost Segers[1], Gaétan Poelman[1,2], Erik Verboven[1], Wim Van Paepegem[1] and Mathias Kersemans[1]

[1] Mechanics of Materials and Structures (UGent-MMS), Department of Materials, Textiles and Chemical Engineering, Ghent University, Technologiepark-Zwijnaarde 46, 9052 Zwijnaarde, Belgium

[2]SIM Program M3 DETECT-IV, Technologiepark-Zwijnaarde 48, B-9052 Zwijnaarde, Belgium

[*]saeid.hedayatrasa@ugent.be

Abstract

Vibrothermography using sinusoidal vibration excitation at the resonance frequencies of a defected area (so-called local defect resonance, or LDR) is a promising technique to boost the defect's deformation and its interfacial interactions and as such enhance resultant vibration-induced heating. Contrary to the classical high-power vibrothermography, low power excitation at an LDR frequency results in a reproducible thermal response and adequate quantification of the corresponding damage features. However, the technique is mainly limited by the fact that it requires a priori knowledge of the LDR frequencies (e.g. obtained from prior vibrational measurements). To overcome this limitation, a stand-alone vibrothermographic spectroscopy procedure is introduced in this paper. The proposed technique applies two consecutive broadband sweep vibrational excitations with ascending and descending frequency modulation rates to the sample. The surface of the excited sample is monitored with an IR camera. Both time derivative analysis and superposition of the recorded thermal responses are performed in order to compensate for the thermal latency of the defect-induced heating. This compensation approach enables proper identification of the actual LDR frequencies based on the apparent LDR frequencies of the thermal response. The method is applied on a carbon fiber reinforced polymer (CFRP) with barely visible impact damage (BVID), and multiple LDR frequencies are readily identified. The identified LDR frequencies are also individually evaluated by both lock-in vibrothermography and 3D scanning laser Doppler vibrometry, confirming the competence of the proposed technique for extracting LDR frequencies in a proper and fast way.

Keywords:

Vibrothermography; Broadband sweep, Local defect resonance (LDR); Thermal latency; BVID; CFRP

1. Introduction

Vibrothermography (also known as sonic thermography or thermosonics) is an active infrared thermography technique in which a defect is detected through its vibration-induced heating [1]. Mechanical vibrations are applied to the test specimen by e.g. an actuator bonded to the surface

which leads to dynamic activation of the defects. The localized strain energy density around the defect and the resultant (normal and tangential) interaction of the defect's interfaces dissipate the vibrational energy as heat. Depending on the orientation, asperities and stress state of the defect, various heating mechanisms come into effect including: rubbing friction, adhesion hysteresis, viscoelastic damping, thermoelastic damping, and even plastic deformation at the crack tips [2-5].

One promising advantage of the vibrothermography is the fact that the dynamic excitation can activate and visualize defect types which are hard to detect through other NDT techniques e.g. kissing bonds and tightly closed cracks [6, 7] or defects oriented normal to the inspection surface [8]. However, adequate activation of the defects such that the resultant vibration-induced heating reaches a detectable limit generally requires a high power excitation, particularly for inspecting composite materials with high damping losses. For this purpose, ultrasonic welding actuators are generally used with a power supply of a few kilowatts [9-11]. The ultrasonic welder vibrates at its optimal frequency and applies a broadband hammer-like load to the sample. This chaotic nature of the loading, makes the experiment irreproducible.

In order to overcome the aforementioned limitations of the classical high power vibrothermography, low power alternatives have been developed recently. The underlying basis of the techniques is to take advantage of the high amplitude vibrations associated with the resonance frequencies inherent to the test piece and/or its damage features. Stimulating resonance mode(s) of the test piece using a shaker can e.g. amplify the self-heating of the sample due to damping losses which shows distinct gradients at the defected areas [12]. Another promising approach is to stimulate resonance modes of the damage features, so-called local defect resonances (LDR), which leads to a highly intensified interaction of interfaces and significantly increases the local vibration-induced heating [13]. In this way various damage features can be selectively activated by tuning the excitation at the corresponding LDR frequency, using a low power piezoelectric (PZT) wafer or even an air-coupled ultrasound transducer [13-17].

Despite the promising efficiency of the LDR based vibrothermography, its application is limited by the fact that the LDR frequencies are required as an input. Hence, the vibrational response of the test piece can be first measured by e.g. a scanning laser Doppler vibrometer (SLDV) to determine the LDR frequencies. The LDR frequencies may be manually extracted from the acquired vibrational spectra, or in an automated manner for which advanced post-processing techniques are under development [18-20]. However, an initial vibrometric identification of the LDRs would naturally make any further vibrothermographic inspection unnecessary. Therefore, it is worthwhile to develop a standalone vibrothermographic approach so that LDRs are more efficiently identified through full-field measurement of the surface temperature.

Rahammer and Kreutzbruck [21] introduced a low power vibrothermography technique with frequency sweep excitation to stimulate any unknown LDR located in the frequency range of excitation. The frequency sweep was performed in a few cycles and the resultant thermal response was post-processed using Fourier transform. Carbon fiber reinforced polymer (CFRP) samples with artificial delaminations were tested and the Fourier analysis at the modulation frequency corresponding to the sweep duration provided an indication of the defects.

In a recent study by the current authors [22], the significant contribution of in-plane LDRs in vibration induced heating was demonstrated. Broadband sweep excitation was applied to impacted CFRP coupons with barely visible impact damage (BVID) and the LDR frequencies with distinct

out-of-plane and in-plane vibrational characteristic were identified using 3D-SLDV measurements. It was shown that the in-plane LDRs can be detected through live monitoring of the surface temperature during the sweep excitation (see supplementary information of [22]).

For further development of the LDR vibrothermography, this paper introduces a vibrothermographic spectroscopy procedure for the effective definition of multiple LDR frequencies solely based on the measured thermal images. The second time derivative of the thermal response is calculated to (i) cancel out the heat dissipation induced by the excitation source, (ii) minimize the in-plane thermal diffusion effects and more importantly (iii) detect the instantaneous gradients of heating intensity due to the activation of LDRs. Moreover, two sweep excitations with ascending and descending linear frequency modulation are applied in order to compensate for the thermal latency in detecting the LDR's thermal signature. Not taking into account this thermal latency, which naturally increases by the depth of the corresponding defect, would lead to erroneous estimation of the LDR frequency.

Prominent LDR frequencies of an impacted CFRP coupon are defined through the proposed vibrothermographic spectroscopy. The advantages of calculating the second time derivative of the thermal response and also the need for compensation of attributed thermal latency are demonstrated. The vibrational response of the sample is measured using a 3D-SLDV and the thermally extracted LDR frequencies are validated.

2. Experimental set-up

A $100 \times 150 \times 5.5\ \mathrm{mm}^3$ CFRP coupon, as shown in Figure 1(a), with the quasi-isotropic lay-up $[(+45/0/-45/90)]_{3s}$ is tested. The sample is impacted with a 7.1 kg drop-weight from a height of 0.1 m according to the ASTM D7136 [23]. The measured impact energy of 6.3 J introduced BVID including a hair-like surface crack at the backside (see the inset of Figure 1(a)). BVID includes a complex combination of various damage features [24], leading to the existence of multiple in-plane and out-of-plane LDRs at the BVID area [22, 25]. The ultrasonic C-scan time-of-flight (TOF) and amplitude images (Figure 1(b,c)) of the impacted CFRP, clearly show the extent and the complex nature of the BVID. The C-scan results are obtained in reflection mode using dynamic time gating and with a focused transducer operated at 5 MHz (H5M, General Electric) [24].

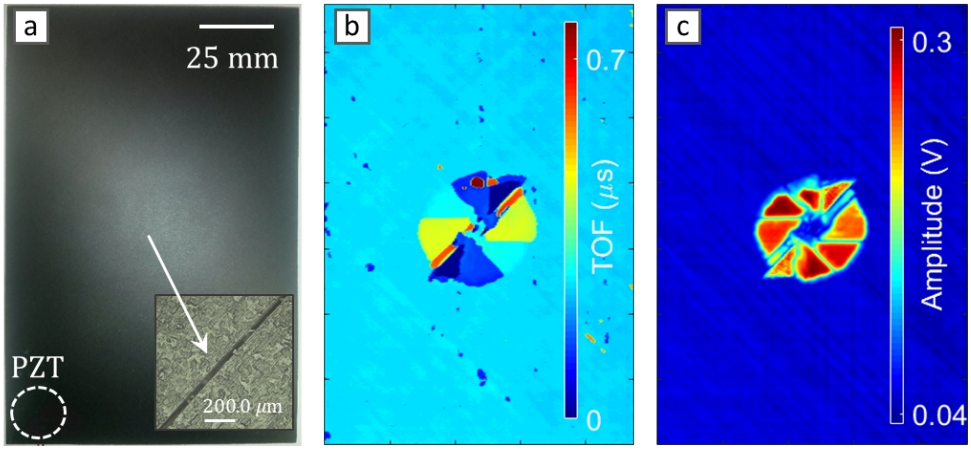

Figure 1. (a) Backside of the impacted CFRP coupon with the quasi-isotropic lay-up $[(+45/0/-45/90)]_{3s}$ and corresponding C-scan (b) time-of-flight (TOF) and (c) amplitude images indicating the BVID

A low power PZT wafer (type EPZ-20MS64W from Ekulit, with a diameter of 12 mm) is glued to the impact side of CFRP coupon (using Phenyl salicylate, or salol) as indicated in Figure 1(a). A function generator together with a Falco System WMA-300 voltage amplifier is used to supply an excitation voltage of 150 Vpp to the PZT. The mechanical power transmitted to the sample by this set-up is calculated about 200 mW [14]. Two linear frequency sweep excitations of each 50 s, with ascending and descending modulation rates within the frequency range 1-250 kHz, are consecutively applied to the sample. The surface temperature is measured by a FLIR A6750sc infrared camera (controlled by edevis GmbH hardware-software) at a sampling rate of 25 Hz. The camera has an array of cryo-cooled InSb detectors, a pixel density of 640×512, a noise equivalent differential temperature (NEDT) of < 20 mK and a bit depth of 14 bit. The temperature is given in digital level (DL) scale, which is the raw output measured by the infrared camera, and which thus corresponds to the intensity of emitted infrared radiation. For the vibrational benchmark study, the vibrational response of the same frequency range (1-250 kHz) is measured using a 3D infrared scanning laser Doppler vibrometer (Polytec PSV-500-3D XTRA). The total measurement time of the SLDV measurement is in the order of 18 minutes.

3. Frequency sweep vibrothermography and thermal response derivative analysis

In this section, the results of both ascending (denoted by ↑) and descending (denoted by ↓) frequency sweep excitations are presented and analyzed. All thermal images are pre-processed by applying cold-image-subtraction (i.e., the temperature T of each pixel is subtracted by its initial value T_0). The ascending frequency sweep is applied first and the temporal mean value of the surface temperature is calculated as shown in Figure 2(a). The image shows the heating of the bottom-left corner of the sample due to the heat dissipation by the PZT wafer and also the LDR-induced heating at the center. For a better interpretation of the results, the colormap is rescaled by excluding the region heated by the PZT, and the defect-induced absolute thermal contrast is calculated as presented in Figure 2(b).

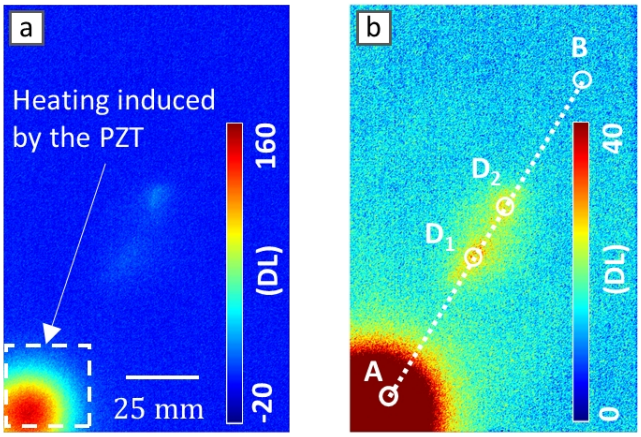

Figure 2. (a) The mean value of measured temperature in digital level (DL) for the ascending sweep excitation and (b) the absolute thermal contrast corresponding to the defected region of interest

For further analysis of the results, the line AB, as indicated in Figure 2(b), is chosen such that it includes the PZT, the sound area, and the points D_1 and D_2 on the two lobes of the defected area. The top row of Figure 3 presents the measured temperature response along the line AB for both ascending and descending frequency sweeps. The curves shown in Figure 3(b,d) correspond to the mean value of circular regions with a diameter of 30 pixels (see the white circles in Figure 2(b)). The temperature gradient at the defected points D_1 and D_2, compared to the non-defected point B, shows a significantly higher heating rate due to the defect-induced heating. Multiple spikes are observed in the thermal response of the defected points due to the momentary contribution of LDRs during the frequency sweep. As expected, the thermal responses of the different defected points are not the same due to their different LDR characteristic. Through comparison of the thermal responses of the ascending frequency sweep (the left column of Figure 3) and the descending frequency sweep (the right column of Figure 3), a symmetric indication of LDR-induced heating is observed around the corresponding frequencies as highlighted by the vertical dash lines.

One may pick the LDR frequencies through the peaks of the thermal response. However, this is not a straight forward approach due to the presence of the measurement noise, intrusion of the heat diffused from surrounding damage features (where other LDRs are activated at earlier time instances), and also the global heating of the sample.

In order to minimize the aforementioned limitations and to obtain an adequate estimate of the peaks corresponding to the LDRs, the second time derivative of the thermal response is calculated. For this purpose, the raw thermal response T of each pixel is first smoothed by Savitzky-Golay filter and then the time derivatives are calculated through the central difference method. The second time derivative of the temperature $\partial^2 T/\partial t^2$, i.e. the curvature of the temperature-time curve in Figure 3(b,d), is a measure for the instantaneous gradient of the heating intensity. Therefore, by analyzing its negative value (i.e. $-\partial^2 T/\partial t^2$) as shown in the bottom row of Figure 3: (i) the peaks indicate time instances at which the maximum gradient of heating intensity is achieved due to the activation of an LDR, and (ii) the dips indicate presences of an inactive LDR (which was already activated, or is going to be activated, at a frequency in the vicinity of the current frequency).

A comparison of the results shown in Figure 3 clearly demonstrates the added value of the second time derivative analysis of the thermal response for the detection of the LDR frequencies.

The thermal trace of the heat dissipated by the PZT and also that of the LDRs excited at the earlier time instances are removed and a clear localized indication of the multiple LDRs is provided. There is a minor indication of the PZT's heating evident at around 200 kHz (see Figure 3(e,g)) which can be explained by the electromechanical anti-resonance mode of the used PZT leading to a small transient deviation in the heating generated by the PZT.

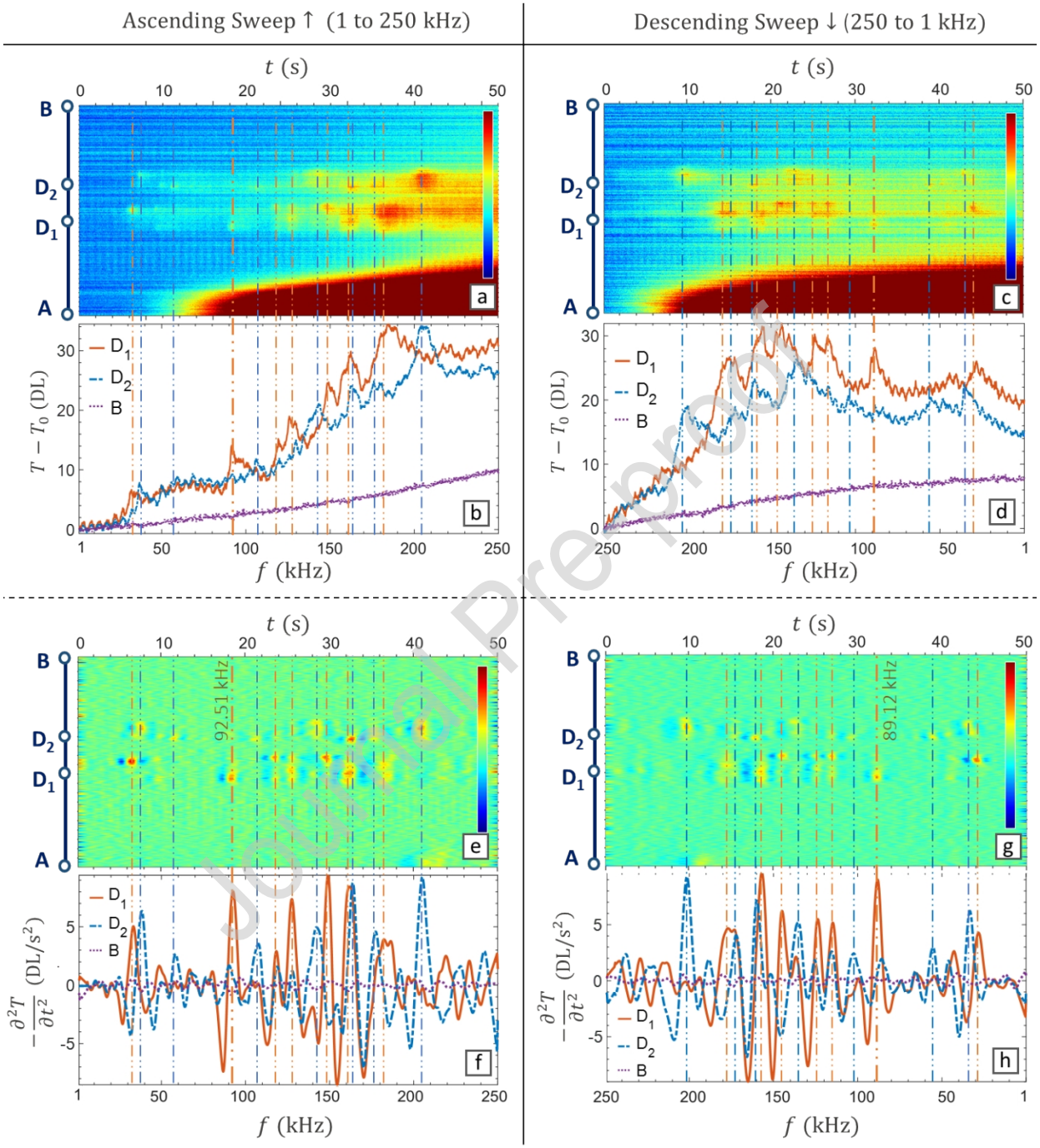

Figure 3. The measured thermal response along the line AB, at the two lobes D_1 and D_2 and also at the non-defected point B (see Figure 2(b)) , (a-d) the raw temperature after cold image subtraction, (e-h) the second time derivative of the temperature

According to Figure 3(f,h), an LDR frequency of around 90 kHz is detected for lobe D_1. However, upon close inspection of the curves, the peaks of ascending and descending frequency sweeps indicate slightly different LDR frequencies of 92.51 kHz and 89.12 kHz respectively. For

further evaluation of this LDR, the time instances associated with both detected frequencies are presented in Figure 4. The top row shows the absolute thermal contrast and the bottom row the corresponding second time derivative. According to Figure 4(a-b), when applying the ascending sweep excitation, lobe D_1 shows a higher temperature compared to D_2 at the frequency 92.51 kHz as suggested by the relevant peak from Figure 3(f).

Likewise, when applying the descending sweep excitation, the lobe D_1 shows a higher temperature compared to D_2 at the frequency 89.12 kHz as suggested by the relevant peak from Figure 3(h). Therefore, it is concluded that an ascending frequency sweep excitation leads to an overestimation of the actual LDR frequency and vice versa. This phenomenon is explained by the latency in the detection of the LDR-induced heat due to the required diffusion time to reach the inspection surface. In case our applied sweep rate would be lower/higher, then the deviation of the apparent LDR frequency from its actual value would decrease/increase. The thermal derivative images shown in Figure 4(a-d) further confirm this observation and provide a much deeper insight about the extent, the intensity and the instantaneous status of the heat generation by the various damage features.

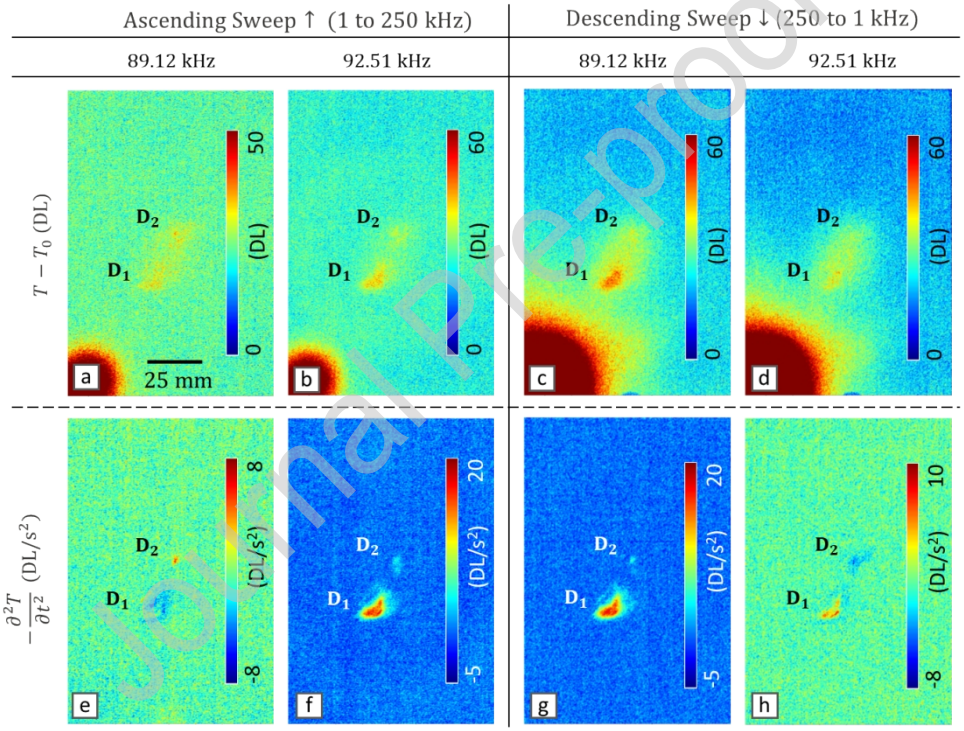

Figure 4. The thermal images at the time instances corresponding to the LDR behavior (the peaks in Figure 3(f) and (h)) observed around 90 kHz, (a-d) the absolute thermal contrast and (e-h) the second time derivative of the temperature

The images in Figure 4(f,g) show one major active pole of heating at D_1 where LDR is expected at the (positive) peaks of $-\partial^2 T/\partial t^2$. Moreover, the images in Figure 4(e,h) show dissimilar and minor bi-polar activity around D_1 and D_2, at frequencies slightly deviated from the relevant peaks of $-\partial^2 T/\partial t^2$. In Figure 4(e), D_1 is an inactive pole at which an LDR is going to be activated or has already been passed, and D_2 is a slightly active pole of the defect which is contributing to the heating. In Figure 4(h), the status of D_1 and D_2 is switched at which the first one is a slightly active pole and the second one is an inactive pole.

4. Superposition of ascending and descending frequency sweep thermal responses and identification of LDR frequencies

In section 3, it was shown that the LDR frequency estimated by the ascending and the descending frequency sweep excitations do not coincide due to the thermal latency attributed in the detection of LDR-induced heating. Whereas the thermal latency of an LDR is the same for both excitations, the following relation is valid between the corresponding time instances:

$$lag_i = t_{\uparrow i} - t_i = t_{\downarrow i} - t_i \tag{1}$$

where lag_i denotes the lag time in detection of the i^{th} LDR, t_i denotes the time instance associated with its actual LDR frequency, and $t_{\uparrow i}$ and $t_{\downarrow i}$ denote the estimated time instances obtained from the ascending and the descending frequency sweep excitations respectively.

Consequently, the following equation can be derived for the relevant frequencies:

$$lag_i = \frac{f_{\uparrow i} - f_i}{k} = \frac{f_{\downarrow i} - f_i}{-k} \tag{2}$$

where k is the constant modulation rate of the linear frequency sweep excitations, and $f_{\uparrow i}$ and $f_{\downarrow i}$ denote the apparent LDR frequencies associated with $t_{\uparrow i}$ and $t_{\downarrow i}$ respectively. Therefore, the actual value of the i^{th} LDR frequency can be approximated as the arithmetic mean value of the pair of apparent LDR frequencies estimated by the two sweep excitations:

$$f_i = \frac{f_{\uparrow i} + f_{\downarrow i}}{2} \tag{3}$$

For this purpose, the second time derivate of the thermal responses of the impacted CFRP calculated for both excitations are superposed as a function of frequency (see Figure 5(a,d)). The pairs of LDR-induced heating peaks as indicated in the superposed curves demonstrate a consistently over-estimation and under-estimation of LDR frequencies by the ascending and descending frequency sweeps respectively. For each of the lobes D_1 and D_2, several peaks exist among which 14 LDR frequencies are picked in total (seven for each lobe), as marked in Figure 5(a,d).

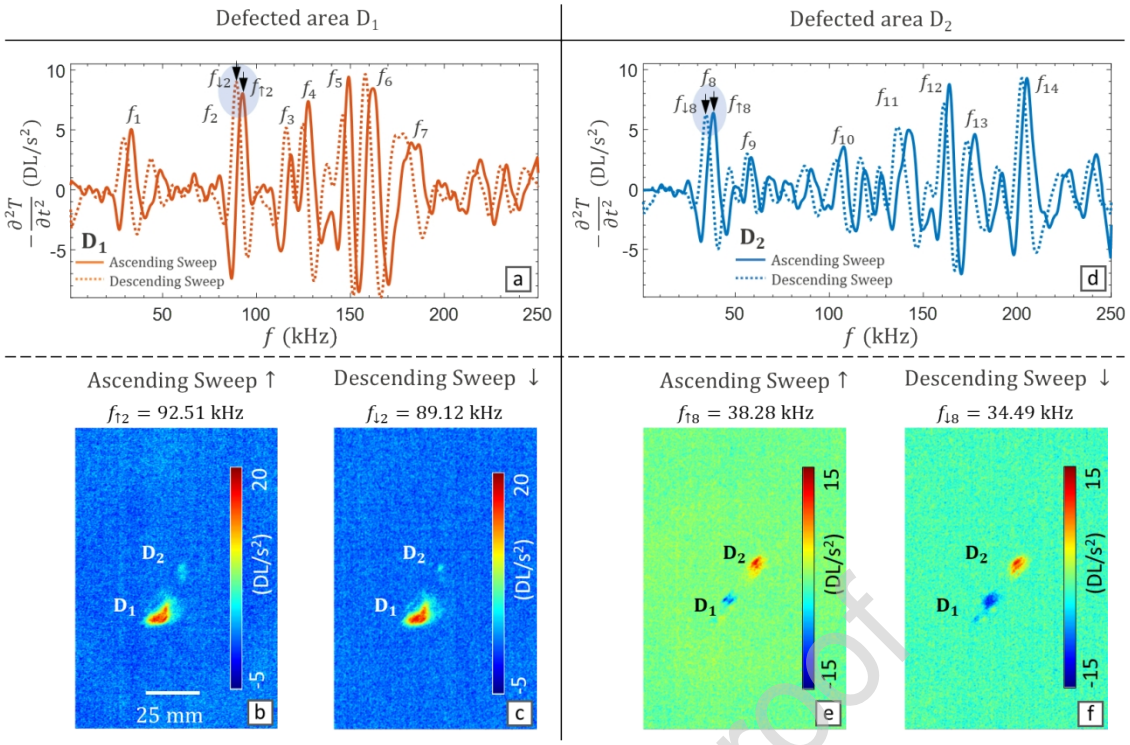

Figure 5. Superposed time derivative results of the ascending and the descending sweeps at (a) D_1 and (d) D_2 , and the relevant full-field maps at the apparent LDR frequencies of (b-c) the 2nd and (e-f) the 8th LDR

The bottom row of Figure 5 shows the full-field images of the second time derivative corresponding to the 2nd LDR (at D_1) and the 8th LDR (at D_2). These full-field images indicate the similarity of the thermal behavior obtained at the two apparent frequencies $f_{\uparrow i}$ and $f_{\downarrow i}$ for the same LDR, in which the considered defected area is the actual active heating pole (indicated by positive values). The selected LDRs indicated in Figure 5(a,d) obtained from the sweep experiments, the corresponding time intervals, and the resultant LDR frequencies are tabulated in Table 1.

Table 1. The LDR frequencies identified from the analysis of the second thermal time derivative as shown in Figure 5(a,d)

Defected region	LDR No. i	$t_{\uparrow i} - t_{\downarrow i}$ (ms)	LDR frequency (kHz)		
			$f_{\uparrow i}$	$f_{\downarrow i}$	$f_i = \frac{f_{\uparrow i} + f_{\downarrow i}}{2}$
D_1	1	801.20	33.30	29.31	31.31
	2	680.72	92.51	89.12	90.82
	3	522.09	118.40	115.80	117.10
	4	562.25	127.60	124.80	126.20
	5	642.57	149.10	145.90	147.50
	6	803.21	161.90	157.90	159.90
	7	1686.75	182.40	1740	178.20
D_2	8	761.04	38.28	34.49	36.39
	9	441.77	58.42	56.22	57.32
	10	883.53	107.70	103.30	105.50
	11	1184.74	142.10	136.20	139.15
	12	602.41	163.90	160.90	162.40
	13	843.37	177.40	173.20	175.30
	14	542.17	205.10	202.40	203.75

5. Validation of LDR frequencies by lock-in vibrothermography and 3D-SLDV vibrometry

This section is dedicated to the validation of LDR frequencies obtained through the proposed vibrothermographic spectroscopy procedure. The two LDRs shown in the bottom row of Figure 5 (i.e. f_2 at D_1, and f_8 at D_2) are further studied and their validity is evaluated through lock-in vibrothermography and 3D-SLDV vibrometry at the corresponding (apparent and resultant) LDR frequencies. The lock-in vibrothermography is performed by exciting the CFRP at the LDR frequencies and applying an amplitude modulation at a frequency of 0.05 Hz for two cycles. For the vibrometry measurements a broadband sweep excitation is applied and the vibrational response corresponding to the LDR frequencies is presented.

The results are presented in Figure 6 and Figure 7 for the selected LDR frequencies f_2 (at D_1), and f_8 (at D_2), respectively. The top row shows the heating amplitude resultant from lock-in vibrothermography, and the bottom row shows the total vibrational velocity amplitude measured by the 3D-SLDV. The three columns from left to right, respectively, show the results corresponding to the apparent frequencies $f_{\uparrow i}$, $f_{\downarrow i}$ and the resultant mean value f_i. The colormap scale of each row is unified, so that the surface maps have the same upper limit corresponding to the maximum magnitude observed at BVID. In this way, among $f_{\uparrow i}$, $f_{\downarrow i}$ and f_i, the frequency leading to the highest vibrational or thermal response can easily be recognized.

Comparison of the results, evidently confirms the fact that the resultant LDR frequency f_i is indeed the best indication of LDR (compared with $f_{\uparrow i}$ and $f_{\downarrow i}$), which manifests much higher vibration-induced heating and also much higher vibrational activation of the relevant lobe at BVID area. The lock-in amplitude at $f_{\uparrow 2}$ (Figure 6(a)) shows dominant heating of D_1 up to 1.4 DL, at $f_{\downarrow 2}$ (Figure 6(b)) it shows heating of D_1 up to 4.2 DL, and at the resultant mean value f_2 (Figure 6(c)) it shows a significantly higher heating at D_1 up to 8.0 DL. This observation is also confirmed by the vibrational velocity of BVID which indicates exclusive LDR behavior at D_1 (Figure 6(d-f)), with low activity at $f_{\uparrow 2}$ (Figure 6(d)) up to 98.6 mm/s and at $f_{\downarrow 2}$ (Figure 6(e)) up to 106.4 mm/s, and the highest activity of 163.6 mm/s at the resultant mean value f_2 (Figure 6(f)).

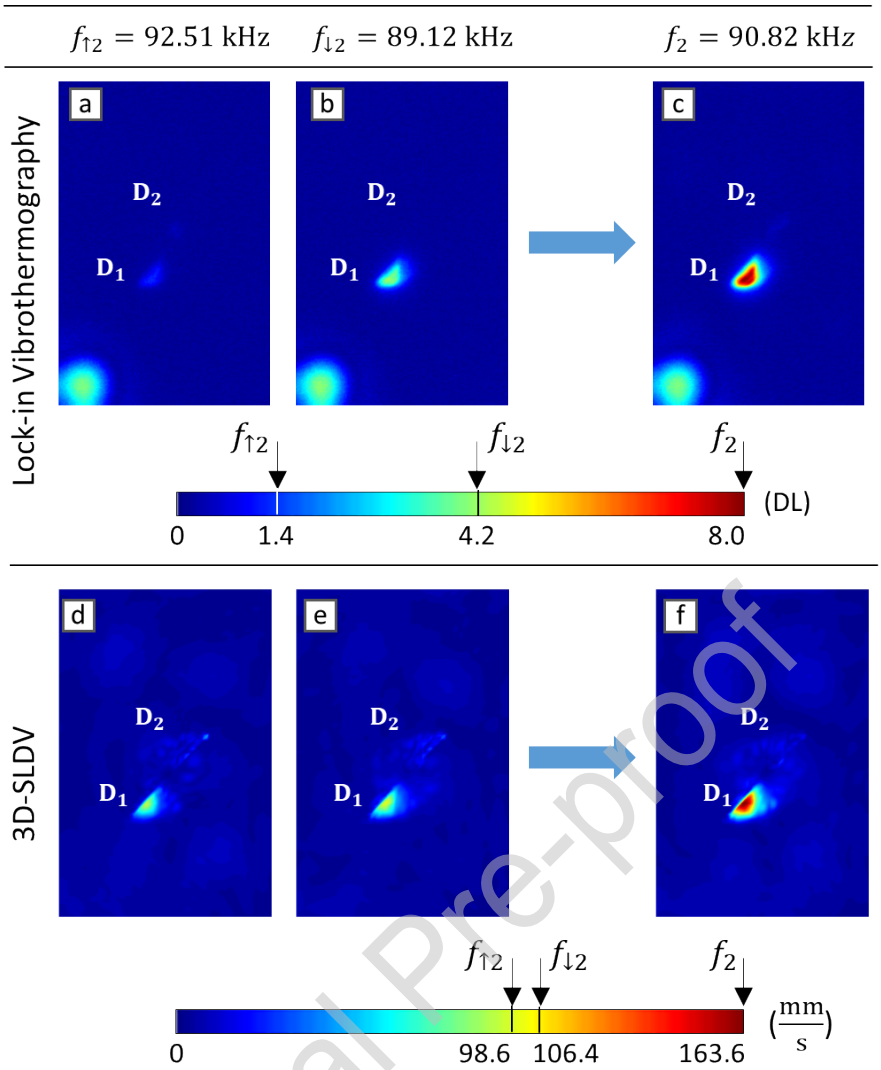

Figure 6. Validation of the selected LDR frequency f_2 corresponding to the lobe D_1 (as shown in Figure 5(a) and listed in Table 1); the arrows on top of the colorbars indicate the maximum magnitude of the measurand in BVID at the apparent and resultant LDR frequencies.

Perhaps even more explicit, the lock-in amplitude at $f_{\uparrow 8}$ (Figure 7(a)) shows equal heating of both lobes of the BVID up to 1.5 DL, at $f_{\downarrow 8}$ (Figure 7(b)) it shows heating of the upper lobe D_2 up to 0.9 DL, and at the mean value f_8 (Figure 7(c)) it shows a much higher heating amplitude of D_2 up to 9.0 DL. This observation is also in excellent agreement with the corresponding vibrational velocity which shows almost equal activation of both lobes at $f_{\uparrow 8}$ up to 36.5 mm/s (Figure 7(d)), slightly dominant activation of the upper lobe D_2 at $f_{\downarrow 8}$ up to 45.7 mm/s (Figure 7(e)), and distinctively higher activation of D_2 at f_8 up to the maximum magnitude of 92.3 mm/s (Figure 7(f)).

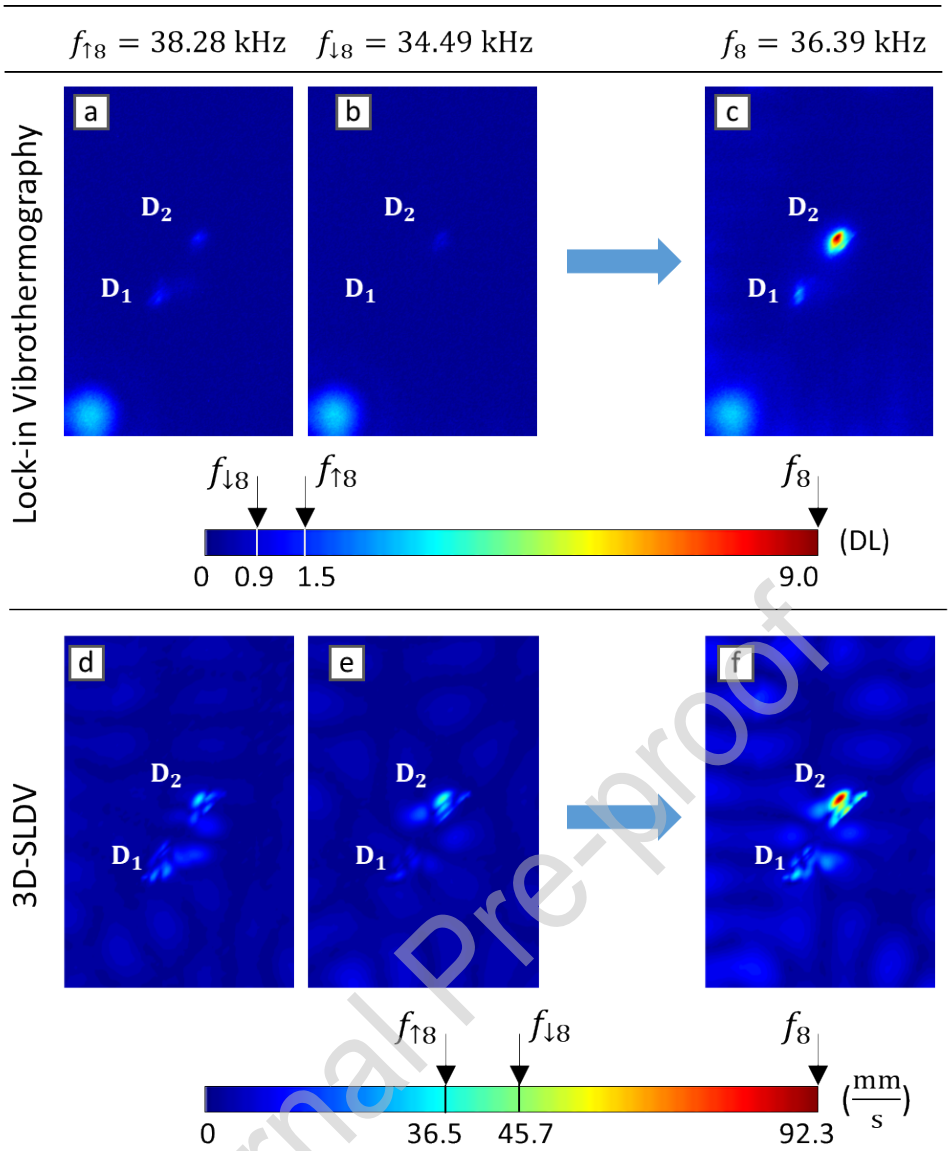

Figure 7: Validation of the selected LDR frequency f_8 corresponding to the lobe D_2 (as shown in Figure 5(a) and listed in Table 1); the arrows on top of the colorbars indicate the maximum magnitude of the measurand in BVID at the apparent and resultant LDR frequencies.

The results evidently indicate that vibrothermographic spectroscopy of a single sweep excitation would yield erroneous LDR frequencies. It is observed that application of such erroneous LDR frequency leads to inefficient LDR activation and therefore inefficient LDR-induced heating in a further lock-in vibrothermography experiment, intended for selective damage quantification. However, superposition of the results obtained from an ascending and a descending sweep, and subsequent compensating for the thermal latency as explained in section 4, will yield the correct identification of LDR frequencies with the highest LDR-induced heating amplitude.

Conclusions

A fast low-power broadband vibrothermographic spectroscopy procedure was introduced for the identification of LDR frequencies from the thermal surface response. The key step in the proposed method is the use of two consecutive linear vibrational sweep excitations with ascending and descending frequency modulation rate. The resultant thermal surface response has been subsequently analyzed by applying the second time derivative.

It was demonstrated that the second time derivative of the thermal response (i) cancels out the heat dissipation induced by the excitation source, (ii) minimizes the in-plane thermal diffusion effects and more importantly (iii) detects the instantaneous gradients of heating intensity due to the transient activation of LDRs during the frequency sweep. It was also shown that the application of both ascending and descending sweeps is crucial to compensate for the thermal latency of the LDR-induced heating, and as such to obtain a correct identification of LDR frequencies.

The proposed method was applied on a CFRP coupon with BVID, and its prominent LDR frequencies were successfully identified. The obtained results were further fully validated by the use of both lock-in vibrothermography and 3D scanning laser Doppler vibrometry.

Acknowledgement

The authors acknowledge the SBO project DETECT-IV (Grant no. 160455), which fits in the SIM research program MacroModelMat (M3) coordinated by Siemens (Siemens PLM software, Belgium) and funded by SIM (Strategic Initiative Materials in Flanders) and VLAIO (Flemish government agency Flanders Innovation & Entrepreneurship). The authors also acknowledge Fonds voor Wetenschappelijk Onderzoek Vlaanderen (FWO-Vlaanderen) through grants 1148018N, 12T5418N and G0B9515N. The authors express their gratitude towards Honda R&D Co. for supplying material for this research.

References

1. Reifsnider, K., E.G. Henneke, and W. Stinchcomb, *The mechanics of vibrothermography*, in *Mechanics of nondestructive testing*. 1980, Springer. p. 249-276.
2. Renshaw, J., et al., *The sources of heat generation in vibrothermography.* NDT & E International, 2011. **44**(8): p. 736-739.
3. Rizi, A.S., et al., *FEM modeling of ultrasonic vibrothermography of a damaged plate and qualitative study of heating mechanisms.* Infrared Physics & Technology, 2013. **61**: p. 101-110.
4. Vaddi, J.S. and S.D. Holland. *Identification of heat source distribution in vibrothermography*. in *AIP Conference Proceedings*. 2014. AIP.
5. Truyaert, K., et al. *Numerical simulation of the heat generation process at vibrating contact defects*. in *14th Quantitative InfraRed Thermography Conference*. 2018. Berlin.
6. Tsoi, K.A. and N. Rajic, *Non-destructive evaluation of aircraft structural components and composite materials at DSTO using sonic thermography*. 2011, Defence Science and Technology Organisation Victoria (Australia) Air Vehicles Div.
7. Roach, D.P. and J. DiMambro, *Enhanced Inspection Methods to Characterize Bonded Joints: Moving Beyond Flaw Detection to Quantify Adhesive Strength*. 2006, Sandia National Lab.(SNL-NM), Albuquerque, NM (United States).
8. Mendioroz, A., et al., *Characterizing the shape and heat production of open vertical cracks in burst vibrothermography experiments.* NDT & E International, 2019. **102**: p. 234-243.
9. Holland, S.D., et al., *Quantifying the vibrothermographic effect.* NDT & E International, 2011. **44**(8): p. 775-782.

10. Guo, X. and V. Vavilov, *Crack detection in aluminum parts by using ultrasound-excited infrared thermography.* Infrared Physics & Technology, 2013. **61**: p. 149-156.
11. Pieczonka, L., et al., *Modelling and numerical simulations of vibrothermography for impact damage detection in composites structures.* Structural Control and Health Monitoring, 2013. **20**(4): p. 626-638.
12. Katunin, A., *A Concept of Thermographic Method for Non-Destructive Testing of Polymeric Composite Structures Using Self-Heating Effect.* Sensors, 2018. **18**(1): p. 74.
13. Solodov, I. and G. Busse, *Resonance ultrasonic thermography: Highly efficient contact and air-coupled remote modes.* Applied Physics Letters, 2013. **102**(6): p. 061905.
14. Solodov, I., et al., *Highly-efficient and noncontact vibro-thermography via local defect resonance.* Quantitative InfraRed Thermography Journal, 2015. **12**(1): p. 98-111.
15. Dyrwal, A., M. Meo, and F. Ciampa, *Nonlinear air-coupled thermosonics for fatigue micro-damage detection and localisation.* NDT & E International, 2018. **97**: p. 59-67.
16. Fierro, G.P.M., et al., *Nonlinear ultrasonic stimulated thermography for damage assessment in isotropic fatigued structures.* Journal of Sound and Vibration, 2017. **404**: p. 102-115.
17. Derusova, D., et al., *Comparing the Efficiency of Ultrasonic Infrared Thermography under High-Power and Resonant Stimulation of Impact Damage in a CFRP Composite.* Russian Journal of Nondestructive Testing, 2018. **54**(5): p. 356-362.
18. Segers, J., et al. *Automated extraction of local defect resonance for efficient non-destructive testing of composites*. in *9th European Workshop on Structural Health Monitoring*. 2018.
19. Segers, J., et al., *Efficient automated extraction of local defect resonance parameters in fiber reinforced polymers using data compression and iterative amplitude thresholding* Sound and Vibration, 2019. **(Under review)**.
20. Roy, S. and T. Bose, *Efficient determination of local defect resonance frequencies from bicoherence plots using double excitations.* Mechanical Systems and Signal Processing, 2019. **127**: p. 595-609.
21. Rahammer, M. and M. Kreutzbruck, *Fourier-transform vibrothermography with frequency sweep excitation utilizing local defect resonances.* NDT & E International, 2017. **86**: p. 83-88.
22. Segers, J., et al., *In-plane local defect resonances for efficient vibrothermography of impacted carbon fiber-reinforced polymers (CFRP).* NDT & E International, 2019. **102**: p. 218-225.
23. D7136/D7136M-15, A., *Standard test method for measuring the damage resistance of a fiber-reinforced polymer matrix composite to a drop-weight impact event*. 2015, ASTM International West Conshohocken, PA.
24. Spronk, S.W.F., et al., *Comparing damage from low-velocity impact and quasi-static indentation in automotive carbon/epoxy and glass/polyamide-6 laminates.* Polymer Testing, 2018. **65**: p. 231-241.
25. Segers, J., et al., *Towards in-plane local defect resonance for non-destructive testing of polymers and composites.* NDT & E International, 2018. **98**: p. 130-133.